

Synchrotron Afterglow Model for AT 2022cmc: Jetted Tidal Disruption Event or Engine-Powered Supernova?

Tatsuya Matsumoto^{1*} and Brian D. Metzger^{1,2}

¹*Department of Physics and Columbia Astrophysics Laboratory, Columbia University, Pupin Hall, New York, NY 10027, USA*

²*Center for Computational Astrophysics, Flatiron Institute, 162 5th Ave, New York, NY 10010, USA*

21 April 2023

ABSTRACT

AT 2022cmc is a luminous optical transient ($\nu L_\nu \gtrsim 10^{45}$ erg s⁻¹) accompanied by decaying non-thermal X-rays (peak duration $t_X \lesssim$ days and isotropic energy $E_{X,\text{iso}} \gtrsim 10^{53}$ erg) and a long-lived radio/mm synchrotron afterglow, which has been interpreted as a jetted tidal disruption event (TDE). Both an equipartition analysis and a detailed afterglow model reveals the radio/mm emitting plasma to be expanding mildly relativistically (Lorentz factor $\Gamma \gtrsim few$) with an opening angle $\theta_j \simeq 0.1$ and roughly fixed energy $E_{j,\text{iso}} \gtrsim few \times 10^{53}$ erg into an external medium of density profile $n \propto R^{-k}$ with $k \simeq 1.5 - 2$, broadly similar to that of the first jetted TDE candidate Swift J1644+57 and consistent with Bondi accretion at a rate $\sim 10^{-3} \dot{M}_{\text{Edd}}$ onto a $10^6 M_\odot$ black hole before the outburst. The rapidly decaying optical emission over the first days is consistent with fast-cooling synchrotron radiation from the same forward shock as the radio/mm emission, while the bluer slowly decaying phase to follow likely represents a separate thermal emission component. Emission from the reverse shock may have peaked during the first days, but whose non-detection in the optical band places an upper bound $\Gamma_j \lesssim 100$ on the Lorentz factor of the unshocked jet. Although a TDE origin for AT 2022cmc is indeed supported by some observations, the vast difference between the short-lived jet activity phase $t_X \lesssim$ days relative to the months-long thermal optical emission, also challenges this scenario. A stellar core-collapse event giving birth to a magnetar or black hole engine of peak duration ~ 1 day offers an alternative model also consistent with the circumburst environment, if interpreted as a massive-star wind.

Key words: transients: tidal disruption events

1 INTRODUCTION

AT 2022cmc was discovered as a luminous, rapidly evolving transient by the Zwicky Transient Facility (Andreoni et al. 2022; Pasham et al. 2022). A potential host galaxy was identified at redshift $z \simeq 1.19$ (luminosity distance $d_L = 8.44$ Gpc), which we adopt hereafter. The optical light curve of AT 2022cmc rose to a peak luminosity $\nu L_\nu \sim 10^{46}$ erg s⁻¹ within a day after its discovery, before decaying by several magnitudes over the course of a week and settling into a slowly-declining “plateau” of luminosity $\sim 10^{45}$ erg s⁻¹ lasting at least a couple of months (hereafter, all times are as measured in the observer frame, unless stated otherwise). While the early rapidly evolving emission was red in color, the later plateau instead exhibited a featureless blue continuum spectrum with a blackbody temperature of $\simeq (2 - 4) \times 10^4$ K and low levels of optical polarization (consistent with zero; Cikota et al. 2023). Multi-wavelength followup starting $\simeq 5$ days after the discovery resulted in the detection of time-variable non-thermal X-ray emission, whose luminosity was rapidly decaying $L_{X,\text{iso}} \simeq 3 \times 10^{47}$ erg s⁻¹ $(t/5 \text{ days})^{-2}$, correspond-

ing to a total radiated energy $E_{X,\text{iso}} \gtrsim 10^{53}$ erg. Observations at radio/mm wavelengths revealed a highly luminous time-evolving source with a synchrotron self-absorbed (SSA) spectrum.

Andreoni et al. (2022); Pasham et al. (2022) interpreted AT 2022cmc as a tidal disruption event (TDE, Hills 1975; Rees 1988) of a star by a supermassive black hole (SMBH) accompanied by a relativistic jet (e.g., Giannios & Metzger 2011; see De Colle & Lu 2020 for a review of jetted TDEs), in part due to the similarity of its non-thermal X-ray and radio emission to previous jetted TDE candidates, particularly the well-studied Swift J1644+57 (Bloom et al. 2011; Burrows et al. 2011; Levan et al. 2011; Zauderer et al. 2011; Wiersema et al. 2012). A TDE association for AT 2022cmc is also supported by the similarity of its blue optical plateau phase with the thermal emission of other better-confirmed TDEs (van Velzen et al. 2019; Hammerstein et al. 2023), including the second jetted TDE candidate Swift J2058+05 (Cenko et al. 2012; Pasham et al. 2015; Wiersema et al. 2020). However, the lack of a confirmed location of AT 2022cmc in the nucleus of the host galaxy (due to the transient outshining the host light), as well as the short peak timescale of the X-ray

* E-mail: tm3238@columbia.edu

emission (\lesssim days)¹ compared to other jetted TDE candidates or to the predicted fallback timescale of the disrupted stellar material (\simeq month for typical SMBH masses $\gtrsim 10^6 M_\odot$), leaves open the possibility for other explanations, particularly the birth of a central engine following the core-collapse of a star (Quataert & Kasen 2012; Nakauchi et al. 2013; Metzger et al. 2015; Perna et al. 2018).

The prototypical jetted TDE candidate Swift J1644+57 exhibited highly time-variable hard X-ray emission lasting roughly $t_x \sim 10$ days after the X-ray trigger, followed by a power-law decay $L_X \propto t^{-5/3}$ similar to the expected late-time mass fallback rate from a TDE (Bloom et al. 2011; Burrows et al. 2011; Levan et al. 2011), which abruptly terminated around $t \simeq 500$ days (Zauderer et al. 2013), possibly as a result of a late-time state transition within the disk (e.g., Tchekhovskoy et al. 2014); a remarkably similar X-ray drop was seen also in Swift J2058+05 (Pasham et al. 2015). The time-lag associated with reverberation mapping of the X-ray spectrum was found to support a SMBH mass of $\sim 10^6 M_\odot$ (Kara et al. 2016; Lu et al. 2017).

As predicted by Giannios & Metzger (2011) just months prior to Swift J1644+57, the onset of the X-ray emission was accompanied by luminous synchrotron radio emission (Zauderer et al. 2011; Berger et al. 2012; Zauderer et al. 2013; Eftekhari et al. 2018; Cendes et al. 2021a), created as the relativistic jet material collided with the sub-parsec scale circumnuclear medium surrounding the (nominally previously quiescent) SMBH. Analysis of the radio emission showed the radiated plasma to be expanding relativistically, with a Lorentz factor $\Gamma \gtrsim few$ (e.g., Zauderer et al. 2011; Metzger et al. 2012; Berger et al. 2012; Barniol Duran & Piran 2013). Although the long-lasting radio emission is well-modeled as originating from the forward shock (FS), a temporal break in the radio light curve around $\sim 2t_x$ was interpreted as evidence for an early reverse shock (RS) phase (Metzger et al. 2012). The radio light curves also exhibited a re-brightening at $t \simeq 1$ month, implying either substantial late-time energy injection into the FS (Berger et al. 2012) and/or complex angular structure of the jet (e.g., a moderately relativistic “sheath” surrounding a high- Γ jet core; Tchekhovskoy et al. 2014; Mimica et al. 2015; Generozov et al. 2017; Lu et al. 2017).

The mechanisms responsible for creating relativistic jets in TDEs remain unclear (e.g., De Colle & Lu 2020 for a review). The discovery of just three jetted TDEs over the past decade—Swift J1644+57, Swift J2058+05, and Swift J1112-82 (Brown et al. 2015)—implies a rate of on-axis jetted TDEs as small as $\sim 0.01 \text{ Gpc}^{-3} \text{ yr}^{-1}$ (Alexander et al. 2020; De Colle & Lu 2020). Allowing for a beaming correction ~ 100 for the jetted X-rays, this implies that only a small fraction $\sim 1\%$ of TDEs create powerful jets; this low jetted TDE fraction is also supported by the lack of radio emission from off-axis jets in the majority of optical and (thermal) X-ray-selected TDEs (Bower et al. 2013; van Velzen et al. 2013; Generozov et al. 2017; Matsumoto & Piran 2021b; however,

¹ It would appear unlikely that the jet was launched well before the epoch of the optical discovery. Such a temporal offset would flatten the X-ray light curve up to roughly the same duration as the offset (Tchekhovskoy et al. 2014), contrary to the observed power-law decay in AT 2022cmc if $t = 0$ is taken at optical discovery.

see Horesh et al. 2021; Perlman et al. 2022; Cendes et al. 2022; Sfaradi et al. 2022; Matsumoto & Piran 2022). The creation of prompt relativistic jets in TDEs via the Blandford-Znajek process (Blandford & Znajek 1977) may require special conditions, such as progenitor stars with atypically strong magnetic fields (e.g., Giannios & Metzger 2011; Bradnick et al. 2017) or a pre-existing active galactic nucleus (AGN) disk threaded by a sufficient magnetic flux (e.g., Tchekhovskoy et al. 2014; Kelley et al. 2014).

In this paper we model the radio and early-time optical emission from AT 2022cmc within the framework of an afterglow model (Giannios & Metzger 2011; Metzger et al. 2012), in order to constrain the properties of the relativistic jet from this event and the density profile of the surrounding gaseous medium. In contrast to Pasham et al. (2022), we assume the early rapidly-declining X-rays arise from emission internal to the jet, as was the interpretation for Swift J1644+57 (e.g., Lu & Kumar 2016; Crumley et al. 2016) and is supported by the rapid X-ray variability time $\sim 10^3$ s. We likewise follow Andreoni et al. (2022) in assuming the blue optical wavelength plateau phase to be thermal emission unrelated to the jet (e.g., originating from the photosphere of the TDE envelope/accretion disk, or the supernova (SN) ejecta in core collapse scenarios).

We begin in §2 by applying basic equipartition arguments to constrain in relatively agnostic terms the properties of the radio emitting region, which we identify as gas behind the FS. Then in §3 we present a detailed synchrotron afterglow light curve calculation, which can explain the early optical emission phase within the same FS model as the radio/mm emission (§3.1). In §4 we discuss some implications of our findings, such as the prediction of an additional RS emission component. We also address the physical origin of AT 2022cmc, comparing the TDE and core collapse scenarios, and their respective implications for the external medium probed by the afterglow. We summarize our conclusions in §5.

2 EQUIPARTITION ANALYSIS

The SSA radio spectrum of AT 2022cmc allows us to estimate the radius and Lorentz factor of the radio emitting region using the equipartition method (Chevalier 1998; Barniol Duran et al. 2013). Using the radio spectra provided by Andreoni et al. (2022) (their Extended Data Fig. 1), we carried out the equipartition analysis within the framework of Matsumoto & Piran (2022) for an assumed on-axis jet orientation. We adopted two scenarios for the geometry of the emitting region: one assumes a narrowly collimated jet with a constant half opening-angle $\theta_j = 0.1$, a choice motivated by observations of jets in AGN (e.g., Pushkarev et al. 2017) and from modeling of Swift J1644+57 (Metzger et al. 2012). In this scenario, as the jet decelerates, we only receive emission from a region of fixed solid angle $\pi\theta_j^2$ (we will see the size of the beaming cone $= 1/\Gamma$ is larger than $\theta_j = 0.1$, where Γ is the Lorentz factor of the emitting shocked gas). The second model assumes a wider jet whose opening angle $\theta_j = 1/\Gamma$ grows as the jet decelerates.

Table 1 shows the results of the equipartition analysis applied to each observational epoch for the two models. Since the spectral fitting by Andreoni et al. (2022) finds that the SSA frequency is always smaller than the characteristic fre-

Table 1. Results of the equipartition analysis (under the assumption of an on-axis viewed emitter) for two scenarios for the jet opening angle of $\theta_j = 0.1$ and $\theta_j = 1/\Gamma$. The quantities Γ , R_{eq} , E_{eq} , E_{tot} , and N_{eq} are the (post-shock) bulk Lorentz factor, radius, energy, outflow’s total energy, and number of emitting particles, respectively. Note E_{eq} here includes only that of the emitting electrons and the magnetic field, which are assumed to be comparable (i.e., $\varepsilon_e \simeq \varepsilon_B$), and E_{tot} includes the energy of hot proton as well taking into account for the deviation from the equipartition with $\varepsilon_e = 0.1$ and $\varepsilon_B = 10^{-3}$ (see also the main text). The observation epochs for which rich data gives relatively secure ν_a and ν_m are shown in boldface.

Observables				Narrow jet ($\theta_j = 0.1$)					Wide jet ($\theta_j = 1/\Gamma$)				
t [day]	F_p [mJy]	ν_a [GHz]	ν_m [GHz]	Γ	R_{eq} [cm]	E_{eq} [erg]	E_{tot} [erg]	N_{eq}	Γ	R_{eq} [cm]	E_{eq} [erg]	E_{tot} [erg]	N_{eq}
5.1	17.2	1.1e+02	1.2e+03	3.1	1.1e+17	1.0e+49	1.4e+50	8.3e+51	1.7	2.6e+16	2.0e+49	2.6e+50	3.0e+52
7.0	12.7	8.2e+01	7.1e+02	3.0	1.3e+17	1.1e+49	1.5e+50	9.6e+51	1.6	3.1e+16	2.1e+49	2.7e+50	3.6e+52
11.6	6.3	5.5e+01	3.6e+02	2.6	1.6e+17	9.5e+48	1.3e+50	1.1e+52	1.4	3.4e+16	2.0e+49	2.5e+50	4.1e+52
15.5	5.0	4.7e+01	2.2e+02	2.5	2.0e+17	9.8e+48	1.3e+50	1.3e+52	1.4	3.9e+16	2.1e+49	2.6e+50	5.0e+52
20.4	4.3	4.0e+01	1.5e+02	2.4	2.4e+17	1.1e+49	1.5e+50	1.6e+52	1.3	4.6e+16	2.3e+49	2.9e+50	6.1e+52
27.8	4.3	3.5e+01	1.2e+02	2.2	2.8e+17	1.4e+49	1.9e+50	2.1e+52	1.3	5.2e+16	3.0e+49	3.8e+50	8.3e+52
45.3	3.1	2.6e+01	1.2e+02	1.9	3.2e+17	1.8e+49	2.4e+50	2.8e+52	1.2	5.4e+16	3.7e+49	4.6e+50	1.0e+53

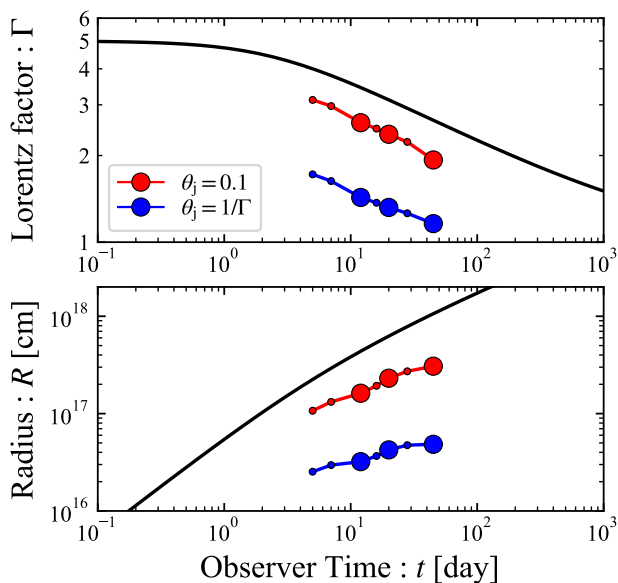


Figure 1. The Lorentz factor (top) and radius (bottom) of the radio emitting region obtained by equipartition analysis. The red and blue points show the results for the models of $\theta_j = 0.1$ (narrow jet) and $\theta_j = 1/\Gamma$ (wide jet), respectively. Large dots represent the epochs for which the break frequencies are best determined due to a good spectral coverage. Black curves show the evolution of the quantities of our afterglow model (see §3.2 for details).

quency, $\nu_a < \nu_m$, the spectrum peaks at ν_m . For the earliest two epochs, the spectral peak F_p is not captured by the frequencies of the observations in Andreoni et al. (2022), so we obtain them by extrapolating their spectral fits assuming a sharp spectral break, which slightly overestimates the peak flux relative to what would be obtained assuming a smooth break. We also remark that the radio/mm data is limited in particular at mm wavelengths, which may allow different

spectral fits.² Nevertheless, our results provide a reasonable physical scenario. Fig. 1 shows the Lorentz factor and radius of the emitting region as a function of time. For both models, the emitting region is found to be mildly relativistic with $\Gamma \simeq 1.5 - 3$ and in a deceleration stage during the observations. The Lorentz factor and radius of the narrow-jet ($\theta_j = 0.1$) model are larger than in the wide-jet model ($\theta_j = 1/\Gamma$) model because the smaller opening-angle requires a larger emitting region to reproduce the observed radio flux.

The equipartition energy E_{eq} , which reflects only the energies (beaming corrected) of emitting electrons and magnetic field, remains almost constant in time $E_{\text{eq}} \simeq 10^{49}$ erg for both scenarios. This implies that the emitting region does not undergo energy injection (or the injection is energetically negligible) at times $\gtrsim 5$ days covered by the radio data. This is despite the fact that the jet (as probed by the variable X-ray emission) does remain active for this period (though the total radiated X-ray energy is dominated by early times; see the next paragraph). By making the “equipartition” assumption, the radius/energy are determined taking the energy of the emitting electrons and the magnetic field to be comparable; while deviations from equipartition do not modify the implied radius and the external density profile significantly, they do increase the required energy considerably (Barniol Duran et al. 2013), a point to which we shall return in §3.1. The number of emitting particles N_{eq} increases weakly in both scenarios.

The temporal evolution of E_{eq} and N_{eq} , as well as the delayed timing of the radio emission relative to the short-lived X-ray emission (taken as a proxy for the jet activity) implicates the radio emission as originating from the FS, i.e., the shocked external medium, as in Swift J1644+57 (e.g., Metzger et al. 2012; Berger et al. 2012). In the case of an adiabatic FS, the energy of the shocked gas remains roughly conserved (absent ongoing energy injection) as the number

² The equipartition quantities weakly depend on the peak flux and frequency. For instance, the quantities in Figs. 1 and 2 obey $\Gamma \propto F_p^{1/5} \nu_p^{-2/15}$, $R_{\text{eq}} \propto F_p^{2/5} \nu_p^{-4/15}$, and $n \propto F_p^{-3/5} \nu_p^{11/15}$. Hence our result is also insensitive to the observables as long as the spectral fit of Andreoni et al. (2022) is reasonably correct.

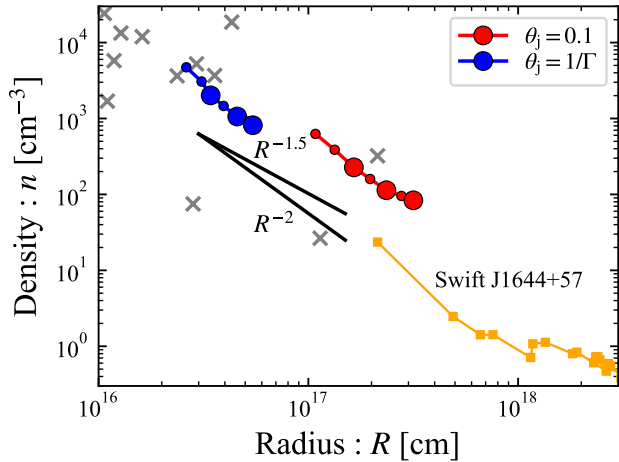


Figure 2. Density profile of the external medium reconstructed by the equipartition method. The orange points represent the profile for Swift J1644+57 taken from Eftekhari et al. 2018. For comparison, gray crosses show the inferred circumstellar-medium density of radio SNe (Chevalier 1998; Chevalier & Fransson 2006, as presented in Bright et al. 2022).

of swept-up particles increases monotonically. The absence of substantial energy injection is supported by the rapidly declining X-ray luminosity, $L_X \propto t^{-2}$, consistent with most of the energy being injected into the blast wave $E \propto \int L_X dt$ occurring prior to the start of the radio observations. In contrast, if the emitting region were the RS passing back through the jet material, the energy of the emitting electrons should increase as more and more particles are swept up. Contrary to Andreoni et al. (2022), we therefore disfavor the RS as the source of the observed radio/mm emission.

Fig. 2 depicts the density profile of the external medium ($n \equiv \rho/m_p$, where ρ is the mass density and m_p the proton mass) under the assumption of a FS origin for the radio emission. The profile for both scenarios is well-described by a power-law in radius R ,

$$n(R) = n_{17} \left(\frac{R}{10^{17} \text{ cm}} \right)^{-k}, \quad (1)$$

where n_{17} is the density at $R = 10^{17}$ cm. The slope implied by the data $k \simeq 1.5 - 2$ (black lines in Fig. 2), is similar to that implied by modeling the early radio emission from Swift J1644+57 (Metzger et al. 2012; Berger et al. 2012) and that from some optical TDEs (e.g., AT 2019dsg, Cendes et al. 2021b; Matsumoto et al. 2022). The density normalization is a factor of at least a few higher in AT 2022cmc than in Swift J1644+57 on a comparable radial scale $\sim 10^{17}$ cm.

3 LIGHT CURVE MODEL

Building on the results of the equipartition analysis, we now construct a detailed synchrotron FS light curve model for AT 2022cmc. We begin with some preliminary considerations, which motivate various aspects of the model, such as the total jet energy and the narrow vs. wide-jet scenario, and which

argue in favor of a FS origin for the early optical emission phase.

3.1 Preliminary Considerations

The distinct shape and red colors of the early optical emission peaking at $t \simeq 1$ day (Andreoni et al. 2022), suggest a separate origin from the bluer thermal plateau phase to follow. Emission from both the FS and RS peaks when the RS crosses the unshocked-jet material (Sari & Piran 1999; Kobayashi 2000; Chevalier & Li 2000; Kobayashi & Zhang 2003) and after which the shocked region begins to decelerate in a self-similar manner (Blandford & McKee 1976); this occurs on a timescale in the observer frame which is roughly commensurate with the active duration of the relativistic jet (i.e. $\lesssim 1$ day in the case of AT 2022cmc if its X-ray emission is indicative). The peak of the early optical phase, which indeed conceivably coincides with the peak of the jetted X-ray phase, may thus be reasonably interpreted as the onset of the FS self-similar deceleration phase, regardless of whether the optical emission originates from the FS or RS.

This deceleration radius is roughly given by

$$R_{\text{dec}} \simeq 2c\Gamma_0^2 t_{\text{dec}} \simeq 6.5 \times 10^{16} \text{ cm} \left(\frac{\Gamma_0}{5} \right)^2 \left(\frac{t_{\text{dec}}}{0.5 \text{ day}} \right), \quad (2)$$

where c is the speed of light, t_{dec} is the deceleration time measured in the engine’s rest frame, and Γ_0 is the Lorentz factor of the emitting region at the deceleration radius. We have normalized Γ_0 to a value = 5, motivated by an extrapolation of the values obtained by the equipartition analysis (Fig. 1) to the optical peak time in the narrow jet scenario ($\theta_j = 0.1$). Using also the inferred external density profile (Eq. 1) we are thus able to estimate the total jet energy:

$$E_{j,\text{iso}} = \frac{4\pi}{3-k} m_p c^2 \Gamma_0^2 R_{\text{dec}}^3 n(R_{\text{dec}}) \quad (3)$$

$$\simeq 9.1 \times 10^{52} \text{ erg} \left(\frac{\Gamma_0}{5} \right)^4 \left(\frac{t_{\text{dec}}}{0.5 \text{ day}} \right) \left(\frac{n_{17}}{300 \text{ cm}^{-3}} \right),$$

where in the second line we have taken $k = 2$. This is comparable to the minimum radiated X-ray energy $E_{X,\text{iso}} \simeq 1.3 \times 10^{53}$ erg, though our model presented in the next section will require larger energies $E_{j,\text{iso}} > E_{X,\text{iso}}$. The beaming-corrected jet energy,

$$E_j = \frac{\theta_j^2}{2} E_{j,\text{iso}} \simeq 5.0 \times 10^{50} \text{ erg} \theta_{j,-1}^2 E_{j,\text{iso},53}, \quad (4)$$

is considerably smaller. Here and hereafter we employ the convention $Q_x = Q/10^x$ for quantities in cgs units except for the density profile normalization n_{17} in Eq. (1).

The net jet energy in Eq. (4) is roughly 10 times larger than the equipartition energy E_{eq} found in the previous section, consistent with the latter representing a lower limit on the total jet energy (also not including an potential hot proton component). A comparison between E_j and E_{eq} can be used to constrain the standard microphysical shock parameters ε_e and ε_B , which represent the ratios of the energies placed into non-thermal electrons and magnetic fields, respectively, relative to the post-shock thermal energy. Following Barniol Duran et al. (2013), for the narrow-jet case we have

$$E_{\text{tot}} \simeq (1 + \varepsilon_e^{-1})^{3/5} \left[\frac{11}{17} \varepsilon^{-2/5} + \frac{6}{17} \varepsilon^{3/5} \right] E_{\text{eq}}, \quad (5)$$

where $\epsilon \equiv (11/6)(\epsilon_B/\epsilon_e)$. Equating E_{tot} with E_j , we thus find

$$\epsilon_B \sim 10^{-3} \epsilon_{e,-1}^{-1/2} \left(\frac{E_{\text{eq}}/E_j}{0.1} \right)^{5/2}, \quad (6)$$

in reasonable accord with the (admittedly loose) constraints on ϵ_B and ϵ_e found in the context of gamma-ray burst (GRB) afterglow modeling (e.g., Ryan et al. 2015).

For the wide spreading-jet scenario ($\theta_j = 1/\Gamma$), the isotropic jet energy becomes $E_{j,\text{iso}} \simeq 5.7 \times 10^{51} \text{ erg } (\Gamma_0/2.5)^4 (n_{17}/300 \text{ cm}^{-3})$, where the initial Lorentz factor $\Gamma_0 \simeq 2.5$ is obtained by extrapolating the equipartition results to early times in the same way as the narrow jet scenario. Insofar that this implies an energy much smaller than the radiated X-ray energy, this disfavors the wide-jet scenario on grounds that it would require an extremely high X-ray radiative efficiency. We note that Eq. (3) can be used to estimate the total energy even if the jet is laterally expanding at $\gtrsim 5$ days unless the jet was already spreading at the initial stage.

Additional information comes from the early optical emission, if interpreted as synchrotron emission from the jet afterglow (e.g., Sari et al. 1998). By fitting a power-law spectrum $F_\nu \propto \nu^\beta$ to the early optical emission, Andreoni et al. (2022) found a best-fit spectral index $\beta = -1.32 \pm 0.18$. Assuming slow-cooling electrons, this implies a power-law distribution $dN/dE \propto E^{-p}$ of non-thermal electron energy with an index $p = 3.64 \pm 0.36$, much steeper than predicted for Fermi acceleration at ultrarelativistic shocks, $p = 2 - 2.2$ (Bell 1978; Blandford & Ostriker 1978; Keshet & Waxman 2005) or found by GRB afterglow modeling, $p \simeq 2 - 3$ (e.g., Fong et al. 2015). In contrast, assuming the optical emission to be in the fast cooling regime gives a more reasonable value, $p = 2.64 \pm 0.36$, consistent with the theoretical prediction and observations. Therefore, we infer the optical emission likely arises from fast-cooling electrons.

Emission from fast cooling electrons disfavors the RS as the origin of the optical emission. The RS light curve peaks when the RS has completely crossed the unshocked-jet material because at this point the number of emitting particles reaches a maximum. After the crossing phase, no additional particles are accelerated, resulting in a sharp cut-off in the spectrum above the cooling frequency. As with the radio/mm emission, the observed power-law decay of the optical light curve after peaking thus favors the FS instead of the RS as the origin of the optical emission. We note that the RS and hence the particle injection may be still present after the optical peak as suggested by the long-lived X-rays. However, if the energy injection rate is proportional to the X-ray luminosity, the predicted decay of the RS luminosity $L_{\text{RS}} \propto L_X \propto t^{-2}$ is steeper than the observed optical decay, unless some additional mechanism acts to offset this decline.

In the fast cooling regime the synchrotron luminosity from the decelerating FS is furthermore independent of the ambient density (e.g., Granot & Sari 2002):

$$\nu L_\nu \stackrel{p=2.6}{\simeq} 9.1 \times 10^{45} \text{ erg s}^{-1} \epsilon_{e,-1}^{p-1} \epsilon_{B,-3}^{\frac{p-2}{4}} E_{j,\text{iso},53}^{\frac{p+2}{4}} \theta_j^2 \left(\frac{\Gamma_0}{5} \right)^2 \left(\frac{t}{\text{day}} \right)^{\frac{2-3p}{4}} \left(\frac{1+z}{2.19} \right)^{\frac{4-p}{2}} \left(\frac{\nu}{5 \times 10^{14} \text{ Hz}} \right)^{-\frac{p}{2}}, \quad (7)$$

where the numerical values are calculated for $p = 2.6$ and have taken into account the suppression factor $(\Gamma\theta_j)^2$ given

Table 2. Model parameters for the synchrotron light curve.

Parameter	Value
n_{17} : Density of external medium at 10^{17} cm^{-3}	200 cm^{-3}
k : Power-law slope of radial density profile	1.8
θ_j : Jet half-opening angle	0.15
$E_{j,\text{iso}}$: Isotropic jet energy	$4 \times 10^{53} \text{ erg}$
Γ_0 : Initial Lorentz factor of shocked gas	5
p : Slope of the electron energy distribution	2.9
ϵ_e : Energy fraction of non-thermal electrons	0.2
ϵ_B : Energy fraction of magnetic field	0.002

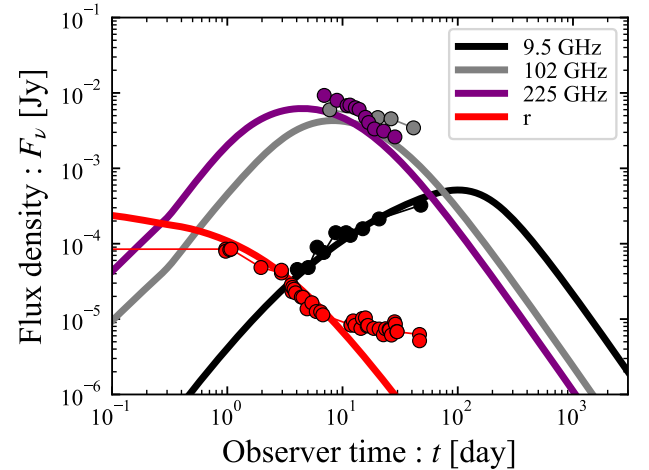


Figure 3. Synchrotron light curve model (lines) fit to the optical/radio data (circles) for AT 2022cmc, considering only emission from the forward shock. The late-time r-band ($\gtrsim 5$ days) likely arises from a separate thermal emission component unrelated to the FS, similar to that observed in Swift J2058+05 and other optically-selected TDEs. The parameters of the model are given in Table 2.

the angular size of the emitting region $\pi\theta_j^2$ for $\theta_j < 1/\Gamma$. The agreement between these predictions and the observed optical flux provides a consistency check on the FS model.

3.2 Light Curve Calculation

Guided by the preliminary considerations in the previous section, we model the light curve of AT 2022cmc assuming the radio and early optical emission both originate from the decelerating FS. The synchrotron light curve is calculated in the same manner as outlined in Bruni et al. (2021); Ricci et al. (2021), but we adopt the prescription of Granot & Sari (2002) to smooth the spectrum and introduce the suppression factor $(\Gamma\theta_j)^2$ on the flux to account for the finite emitting size of the jet, as mentioned above. The parameters of the model are summarized in Table 2, with several of their values already motivated by the analysis in the previous section.

Fig. 3 depicts a light curve model that reasonably reproduces the radio and optical data, which we show for comparison with circles. The adopted parameter values of this model (Table 2) were found heuristically by exploring val-

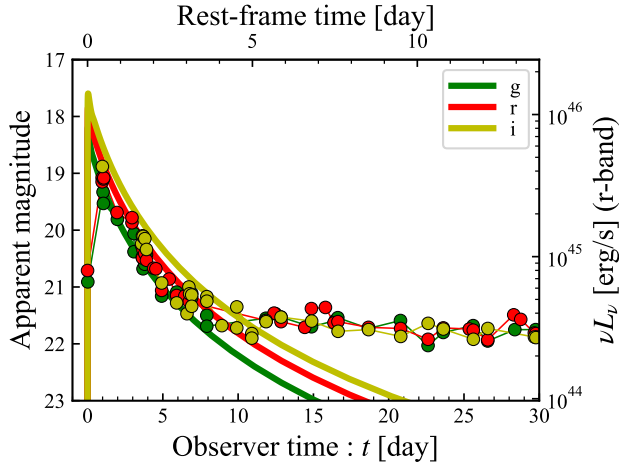


Figure 4. Optical light curves for AT 2022cmc compared to our synchrotron afterglow model. The right vertical axis denotes the luminosity for r-band. The luminosities at g and i-bands are roughly 1.34 and 0.88 times larger than the r-band luminosity.

ues around those hinted by the equipartition analysis, rather than through a systematic parameter scan. Fig. 4 shows just the optical data, now broken down into separate colors. As already mentioned, the light curve is comprised of two parts: an early red peak followed by blue plateau (Andreoni et al. 2022; Pasham et al. 2022). Insofar as the late plateau ($\gtrsim 5$ days) is better described as thermal emission of temperature $\simeq (2 - 4) \times 10^4$ K similar to optical TDEs (van Velzen et al. 2021; Hammerstein et al. 2023), we ignore this component and focus on fitting just the early peak phase.

Figs. 5 and 6 show, respectively, the radio spectrum of the model and the data at each epoch and the time evolution of key synchrotron break frequencies. Although our favored model largely agrees with the observations (within a factor of a few) at most epochs, there is a noticeable discrepancy in the late-time spectrum near day 45.3. Around ~ 100 GHz, our theoretical spectrum underestimates the observed flux by a factor of 3 – 4. We speculate that this excess could reflect additional contributions to the observed emission from different angular portions of the jet FS not captured by our one-zone model (e.g., the “sheath” surrounding the jet core; Mimica et al. 2015; Genozov et al. 2017) or energy injection from slower material gradually catching up with the FS region (Berger et al. 2012), as was previously proposed to explain the late-time brightening in Sw J1644+57. Future observations will test this possibility.

Combining the isotropic jet energy $E_{j,\text{iso}}$ of our reasonably good-fitting model with the measured X-ray energy $E_{X,\text{iso}}$, we can constrain the prompt radiative efficiency of the jet,

$$\varepsilon_X \equiv \frac{E_{X,\text{iso}}}{E_{j,\text{iso}} + E_{X,\text{iso}}} \gtrsim 0.2, \quad (8)$$

where we have used $E_{j,\text{iso}} = 4 \times 10^{53}$ erg and $E_{X,\text{iso}} = 10^{53}$ erg. The latter (and hence also ε_X) is a lower-limit because the X-ray luminosity $L_X \propto t^{-2}$ had already begun decaying by the time observations commenced at $t \simeq 5$ days. The extrapolation of this luminosity to $t \simeq 1$ day results in the X-ray energy of $E_{X,\text{iso}} \simeq 5 \times 10^{53}$ erg and relatively high emission

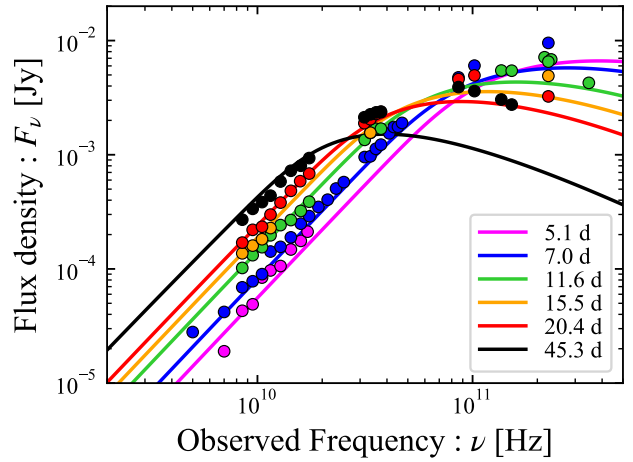


Figure 5. Radio spectrum of AT 2022cmc at each epoch (times measured in the observer frame; from Andreoni et al. 2022) compared to our model predictions.

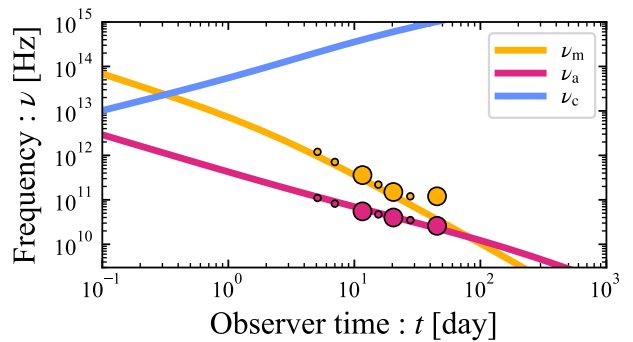


Figure 6. Time evolution of the characteristic synchrotron (ν_m), SSA (ν_a), and cooling (ν_c) frequencies based on fitting the observed radio/mm spectrum, compared to the model predictions.

efficiency of $\varepsilon_X \simeq 0.6$, comparable to that found for Swift J1644+57, $\varepsilon_X \simeq 0.5$ (Berger et al. 2012) and the gamma-ray efficiencies of GRBs ($\varepsilon_\gamma \simeq 0.4 - 0.6$, Fong et al. 2015, but see also Beniamini et al. 2016).

4 DISCUSSION

4.1 Early Reverse Shock Emission

While our analysis favors the FS instead of the RS as the origin of the radio/mm and early optical emission from AT2022cmc, the RS may still generate observable emission. This will occur on timescales ~ 1 day, comparable to the duration of the X-ray/optical peak, when the RS is crossing the bulk of the jet material and its emission reaches a maximum (Sari & Piran 1999; Kobayashi 2000). The RS emission offers a potential probe of the unshocked jet material (Giannios & Metzger 2011; Metzger et al. 2012), particularly its bulk Lorentz factor and magnetization. In this section we discuss

the detectability of the RS emission and the implications of its presence or absence in AT 2022cmc and similar future events.

During the RS crossing phase, the Lorentz factor of the post-shock gas Γ_{sh} and the Lorentz factor of the RS relative to the unshocked jet $\tilde{\Gamma}_{\text{RS}}$, are determined by two parameters (Sari & Piran 1995). One is the Lorentz factor of the unshocked jet, Γ_j , and the other is the density ratio of the unshocked-jet material to the external medium:

$$f \equiv \frac{n_j}{n_{\text{ext}}} \simeq 5.9 L_{j,\text{iso},48} \Gamma_{j,1}^{-2} \left(\frac{n_{17}}{300 \text{ cm}^{-3}} \right)^{-1}, \quad (9)$$

where the comoving density of the unshocked jet with kinetic power $L_{j,\text{iso}}$ is given by

$$n_j = \frac{L_{j,\text{iso}}}{4\pi R^2 m_p c^3 \Gamma_j^2} \simeq 1800 \text{ cm}^{-3} L_{j,\text{iso},48} \Gamma_{j,1}^{-2} R_{17}^{-2}, \quad (10)$$

and we have adopted the external density profile (Eq. 1) with $k = 2$, making f conveniently independent of radius.

For $\Gamma_j^2 \gg f$, the RS is relativistic and the Lorentz factors of the RS and shocked material are given by

$$\tilde{\Gamma}_{\text{RS}} \simeq \left(\frac{\Gamma_j^2}{4f} \right)^{1/4} \simeq 1.4 \Gamma_{j,1} L_{j,\text{iso},48}^{-1/4} \left(\frac{n_{17}}{300 \text{ cm}^{-3}} \right)^{1/4}, \quad (11)$$

$$\Gamma_{\text{sh}} \simeq \Gamma_j \left(\frac{f}{4\Gamma_j^2} \right)^{1/4} \simeq 3.5 L_{j,\text{iso},48}^{1/4} \left(\frac{n_{17}}{300 \text{ cm}^{-3}} \right)^{-1/4}. \quad (12)$$

Note that Γ_{sh} is independent of Γ_j , and roughly coincides with initial Lorentz factor of the FS-emitting material defined earlier, Γ_0 . In particular, the fiducial value of our FS afterglow model $\Gamma_0 = 5$ (Table 2) is obtained for $L_{j,\text{iso}} \simeq 2.8 \times 10^{48} \text{ erg s}^{-1}$ ($n_{17}/200 \text{ cm}^{-3}$), consistent with $L_{j,\text{iso}} \simeq E_{j,\text{iso}}/t_j$ given the total jet energy $E_{j,\text{iso}} \sim 10^{53} \text{ erg}$ and peak jet duration $t_j \sim 1 \text{ day}$.

The top panel of Fig. 7 depicts both Γ_{sh} and $\tilde{\Gamma}_{\text{RS}}$ as a function of Γ_j obtained by solving the exact shock jump condition in Sari & Piran (1995). To obtain the shocked Lorentz factor of 5 indicated by our FS afterglow analysis, the Lorentz factor of the unshocked jet is constrained to obey $\Gamma_j \gtrsim 10$, similar to inferred for Swift J1644+57 (e.g., Metzger et al. 2012). While Γ_{sh} is independent of Γ_j , the RS Lorentz factor increases with Γ_j , rendering the RS emission sensitive to its value. In particular, the RS becomes relativistic for

$$\Gamma_j \gtrsim \Gamma_{j,\text{cr}} \simeq 14 L_{j,\text{iso},48}^{1/4} \left(\frac{n_{17}}{300 \text{ cm}^{-3}} \right)^{-1/4}. \quad (13)$$

We now estimate the SED of the RS emission from AT 2022cmc at its peak, which as already mentioned is expected to coincide with the early optical peak at $t \sim 1 \text{ day}$. This is done by considering the ratio between the characteristic synchrotron frequency and luminosity of the FS versus the RS. Assuming the same microphysical parameter ε_B for both the FS and RS, the magnetic field strength of the post-shock gas will also be identical due to the pressure equilibrium across the contact discontinuity; the bulk Lorentz factor of the emitting gas Γ_{sh} behind both shocks is also the same. However, the random Lorentz factors of the electrons behind the FS and RS differ because of their different respective shock strengths (shock Lorentz factors). Taking these points into account, the ratio of the characteristic frequencies of the FS to RS emission can be estimated as (e.g., Giannios & Metzger 2011)

$$\frac{\nu_{m,\text{RS}}}{\nu_{m,\text{FS}}} = \frac{(\tilde{\Gamma}_{\text{RS}} - 1)^2}{(\Gamma_{\text{sh}} - 1)^2} \simeq 0.17 \Gamma_{j,1}^2 L_{j,\text{iso},48}^{-1} \left(\frac{n_{17}}{300 \text{ cm}^{-3}} \right), \quad (14)$$

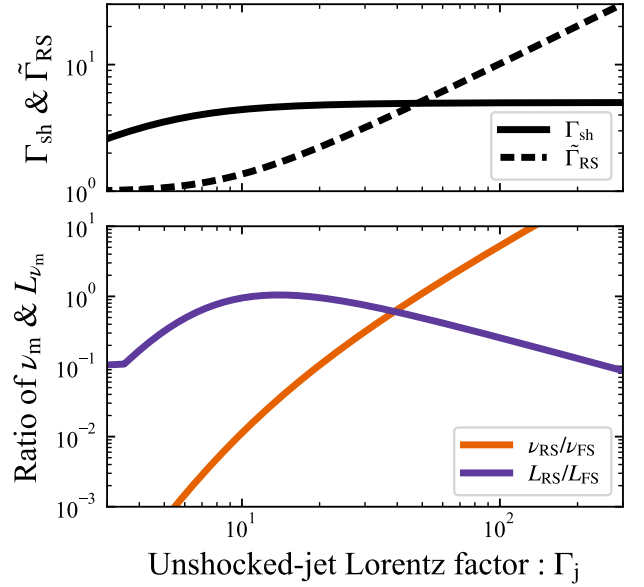


Figure 7. (Top) Lorentz factors of the shocked jet material (Γ_{sh} , solid) and the RS ($\tilde{\Gamma}_{\text{RS}}$, dashed) as a function of the unshocked-jet Lorentz factor Γ_j . The parameters are set as $L_{j,\text{iso}} = 2.8 \times 10^{48} \text{ erg s}^{-1}$ ($n_{17}/200 \text{ cm}^{-3}$) so that $\Gamma_{\text{sh}} = 5$ for $\Gamma_j \gg 10$ (see Eq. 12). (Bottom) Ratios of the characteristic synchrotron frequency (ν_m , orange) and luminosity (L_{ν_m} , purple) of the RS to FS.

where the last equality holds only for $\Gamma_j > \Gamma_{j,\text{cr}}$. The bottom panel of Fig. 7 depicts the behavior of this ratio as a function of Γ_j .

Since the synchrotron emissivity is the same for both the FS and RS emission regions, and assuming the electrons behind both shocks are in a slow-cooling regime, the ratio of their luminosities at ν_m can be obtained by considering the number of accelerated particles at each. At the peak of the FS, the number of particle in the post FS region is given by the particles swept up by the FS, $\sim E_{j,\text{iso}}/(m_p c^2 \Gamma_{\text{sh}}^2)$. For the RS, the number is given by the particles within the shell $\sim E_{j,\text{iso}}/(m_p c^2 \Gamma_j)$. Therefore, the luminosity ratio is given by

$$\frac{L_{\nu_m,\text{RS}}}{L_{\nu_m,\text{FS}}} \simeq \frac{\Gamma_{\text{sh}}^2}{\Gamma_j} \simeq 1.2 \Gamma_{j,1}^{-1} L_{j,\text{iso},48}^{1/2} \left(\frac{n_{17}}{300 \text{ cm}^{-3}} \right)^{-1/2}. \quad (15)$$

Again, the last equality holds for $\Gamma_j > \Gamma_{j,\text{cr}}$. We show this ratio as a function of Γ_j in the bottom panel of Fig. 7. It should be noted that when the shock becomes Newtonian and its velocity becomes smaller than a critical value $v_{\text{DN}} \simeq 0.2 c \varepsilon_{e,-1}^{-1/2}$ for $p = 2.6$, the minimal random Lorentz factor becomes a few and the so-called deep Newtonian regime sets in (Huang & Cheng 2003; Sironi & Giannios 2013). In this regime, the number of the accelerated particles is suppressed relative to the standard case by a factor of $\simeq (v/v_{\text{DN}})^2$, where v is the shock velocity. This effect is included in our calculation and is responsible for the break in the luminosity ratio at $\Gamma_j \simeq 3$ in Fig. 7.

We estimate the SED of the RS near the time of the optical peak in Fig. 8. The characteristic frequency ν_m and its luminosity L_{ν_m} are obtained by scaling those of the FS according to Eqs. (14) and (15). We account for suppression of

the flux due to SSA at the RS as well as the FS. We find for sufficiently large jet Lorentz factors $\Gamma_j \gtrsim 30$, SSA at the RS does not contribute to shaping the spectrum as much as the FS, due to the lower density and higher temperature of the former. For even larger jet Lorentz factor $\Gamma_j \gtrsim 100$, the RS may in fact dominate the optical emission, contrary to our earlier inference that the optical emission in AT 2022cmc is likely to be dominated by the FS (§3.1). In the fast cooling regime, the luminosity is estimated by using Eq. (7), which holds after the beginning of the deceleration, and Eq. (12) for Γ_0 and scaling relations of (14) and (15),

$$(\nu L_\nu)_{\text{RS}} \stackrel{p=2.6}{\simeq} 2.6 \times 10^{45} \text{ erg s}^{-1} \varepsilon_{e,-1}^{p-1} \varepsilon_{B,-3}^{\frac{p-2}{4}} E_{j,\text{iso},53}^{\frac{p+2}{4}} \theta_{j,-1}^2 \Gamma_{j,1}^{p-2} L_{j,\text{iso},48}^{\frac{3-p}{2}} \left(\frac{n_{17}}{300 \text{ cm}^{-3}} \right)^{\frac{p-3}{2}}, \quad (16)$$

where we have omitted the dependence on t , z , and ν , which are the same as for Eq. (7). Note this equation is valid for $\nu_{\text{m,RS}} < \nu_c$ and $\Gamma_j > \Gamma_{j,\text{cr}}$. The non-detection of an extra component in the optical light curve thus places a weak upper limit on the unshocked jet Lorentz factor for our fiducial parameters in Table 2:

$$\Gamma_j \lesssim 100 \left(\frac{\varepsilon_e}{0.2} \right)^{-\frac{p-1}{p-2}} \left(\frac{\varepsilon_B}{0.002} \right)^{-\frac{1}{4}} \left(\frac{E_{j,\text{iso}}}{4 \times 10^{53} \text{ erg}} \right)^{-\frac{p+2}{4(p-2)}} \left(\frac{\theta_j}{0.15} \right)^{-\frac{2}{p-2}} \left(\frac{L_{j,\text{iso}}}{2.8 \times 10^{48} \text{ erg s}^{-1}} \right)^{\frac{p-3}{2(p-2)}} \left(\frac{n_{17}}{200 \text{ cm}^{-3}} \right)^{-\frac{p-3}{2(p-2)}}. \quad (17)$$

Finally, we note that our analysis has assumed a jet that is relatively weakly magnetized, by the deceleration radius $\sim 10^{17}$ cm (Eq. 2). In the jet were instead to remain highly magnetized, the jet energy is still transferred from the FS and its emission remains largely unchanged; however, the strength of the RS and hence its luminosity can be strongly suppressed relative to our estimates here for a highly magnetized jet (e.g., Zhang & Kobayashi 2005; Giannios et al. 2008).

4.2 The Origin of AT 2022cmc

Although AT 2022cmc was interpreted as a jetted TDE (Andreoni et al. 2022; Pasham et al. 2022), there are reasons to be cautious about this connection. One is that the location of the transient within its host galaxy is not yet resolved, making a nuclear origin impossible to confirm, at least until the transient has faded. Secondly, the inferred duration of the jetted activity, as implied by the length of the early optical and X-ray emission phase, is over an order of magnitude shorter than the typical fallback timescale \gtrsim weeks of the stellar debris in a TDE for a typical SMBH mass $\sim 10^6 M_\odot$. This timescale problem could be alleviated by invoking a much lower-mass (e.g. intermediate mass) black hole, or by considering the tidal disruption of a white dwarf instead of a main-sequence star (e.g., Krolik & Piran 2011); however, these scenarios are not obviously consistent with the \gtrsim months-long duration of the thermal optical emission assuming the latter is also powered by accretion onto the SMBH (see below).

Nevertheless, the luminous blue optical plateau phase, whose colors and estimated bolometric luminosity of $\sim 10^{45}$ erg s $^{-1}$ are indeed similar to those observed in optically-selected TDEs (e.g. van Velzen et al. 2021; Hammerstein et al. 2023) as well as the jetted TDE candidate Swift J2058+05

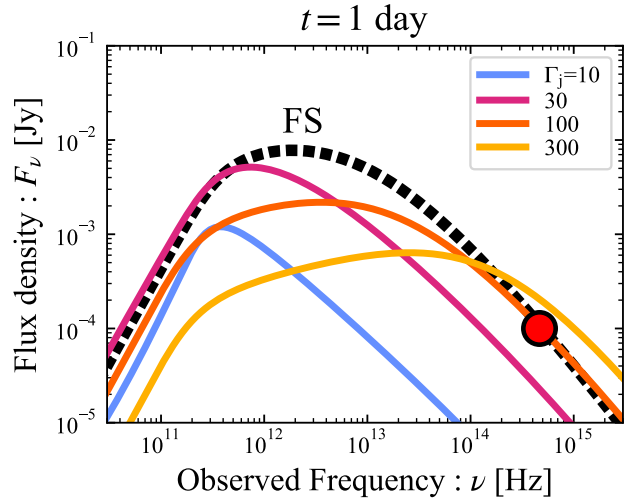


Figure 8. The estimated SED of the RS emission from AT 2022cmc at 1 day, when it reaches peak luminosity around the time of the optical maximum. The red point denotes the observed r-band flux at this epoch.

(Cenko et al. 2012), but not consistent with most other transient classes. Such high luminosity events are still rare among the optically-selected TDE population and are indeed characterized by spectra lacking emission or absorption lines (Hammerstein et al. 2023), qualitatively similar to the featureless spectrum of the plateau phase in AT 2022cmc (Andreoni et al. 2022). Extremely luminous TDEs are challenging to explain in models for TDE optical emission which invoke shocks between tidal debris streams (e.g., Piran et al. 2015; Ryu et al. 2020)³ and the specific implication in AT 2022cmc that efficient accretion onto the SMBH has already begun for the jet to be launched.⁴ The large luminosity is also in tension with reprocessing wind models (e.g., Metzger & Stone 2016; Dai et al. 2018; Lu & Bonnerot 2020) due to the large required ejecta mass (Matsumoto & Piran 2021a).

In the “cooling envelope” emission model (Metzger 2022; see also Coughlin & Begelman 2014), TDE thermal optical emission originates from a quasi-spherical hydrostatic envelope radiating near the SMBH Eddington limit, which to explain the observed optical plateau luminosity $\simeq 10^{45}$ erg s $^{-1}$ of AT 2022cmc would require a SMBH mass $M_{\text{BH}} \sim 10^7 M_\odot$. To reproduce the long duration of the optical phase \gtrsim months if interpreted as the Kelvin-Helmholtz cooling time of the envelope, would require the disruption of a massive star $m_* \gtrsim 10 M_\odot$. Alternatively, a plateau light curve phase is generated if the SMBH accretion flow continually resupplies the envelope with energy in a regulated manner; however, the required long-lived accreting SMBH engine is again chal-

³ Following analytic estimates presented in Ryu et al. (2020), we find that reproducing a peak luminosity $\sim 10^{45}$ erg s $^{-1}$ would require the disruption of an exceptionally massive $m_* \gtrsim 100 M_\odot$ star.

⁴ It should be noted that these bright featureless TDEs with radiated energy of $\sim 10^{52}$ erg are free from the inverse energy crisis advocated for optical TDEs (Piran et al. 2015; Svirski et al. 2017).

lenged by the much shorter jet activity period suggested by the X-ray emission.

An alternative model for AT 2022cmc is the core collapse of a massive star that gives birth to an energetic central compact object, such as a millisecond magnetar (e.g., Thompson et al. 2004) or accreting black hole (e.g., Quataert & Kasen 2012; Dexter & Kasen 2013; Perna et al. 2018). A magnetar engine rotating near its break-up velocity (spin period $P \sim 1$ ms) with a long energy injection (e.g., dipole spin-down) timescale $t_{\text{sd}} \sim 1$ day, was proposed by Metzger et al. (2015) to explain Swift J2058+05 and the extremely luminous transient ASASSN-15lh (Dong et al. 2016; also claimed to be a TDE by Leloudas et al. 2016); a portion of the magnetar’s spin-down energy goes into a bipolar relativistic jet of active duration t_{sd} which is capable of breaking through the expanding stellar envelope (e.g., Margalit et al. 2018) while the remainder is thermalized behind the ejecta, powering extremely luminous SN emission (e.g., Kasen & Bildsten 2010; Woosley 2010; Vurm & Metzger 2021). A similar jetted-engine-boosted SN scenario was proposed by Metzger et al. (2015) to explain the over-luminous SN 2011kl associated with the ultra-long GRB 111209A (Greiner et al. 2015).

Fig. 9 shows an example light curve model in the engine-powered SN scenario for AT 2022cmc. We adopt a simple one-zone model as Metzger et al. (2015) but with an energy injection rate to the ejecta from the central engine following $L_{\text{inj}} = 10^{47}/[1 + (t/\text{day})^2]$ erg s $^{-1}$ (dashed line) motivated by the X-ray light curve (purple line). The ejecta mass and opacity are set to $M_{\text{ej}} = 3 M_{\odot}$ and $\kappa = 0.1 \text{ cm}^2 \text{ g}^{-1}$, respectively. The SN component can broadly reproduce the blue plateau up to ~ 100 days, though color evolution resulting from the ejecta cooling is inevitable in a supernova model. The initial kinetic energy is $E_{\text{kin},0} = 10^{51}$ erg, but the result does not depend on this precise value as long as it is smaller than the injected energy $E_{\text{kin},0} < E_{\text{inj}} \simeq 10^{52}$ erg. Since the peak luminosity is roughly the same as the luminosity injected by the engine at the diffusion time $\sim \sqrt{\frac{3\kappa M_{\text{ej}}}{4\pi c v_{\text{ej}}}}$ (Arnett 1982), the peak time of $\simeq 30$ days constrains the ejecta mass $M_{\text{ej}} \simeq 3 M_{\odot} E_{\text{inj},52}^{1/3} \kappa_{-1}^{-2/3}$. Given the adopted injection luminosity of $\simeq 10^{47}$ erg s $^{-1}$ at 1 day and the extrapolated X-ray luminosity of $\simeq 8 \times 10^{48}$ erg s $^{-1}$ at 1 day with the inferred efficiency of $\varepsilon_{\text{X}} \simeq 0.6$ and the beaming fraction of $\sim 10^{-2}$, we find the central engine must share its energy roughly equally between its relativistic jet and that going into SN heating. Such a partition is realized by dissipation of the striped wind in a millisecond magnetar scenario if the magnetic dipole is misaligned with the rotation axis by an angle $\simeq 0.4$ (Margalit et al. 2018).

We comment that such rapid magnetar birth spin periods ~ 1 ms are challenging to explain from binary star evolution models which include updated angular momentum transport schemes (Fuller & Lu 2022). Chemically homogeneous single-star models may fare better, though the necessarily high mass of such progenitors would likely require a larger SN ejecta mass $\gtrsim 10 M_{\odot}$ than our example model in Fig. 9. On the other hand, our spherically-symmetric model could overestimate the light curve evolution timescale (and hence underestimate the ejecta mass) for a viewer along the rotation axis, where the expansion velocity is higher than the average. For an accreting black hole scenario, the long jet duration $\gtrsim 5$ days requires a long fallback timescale for the

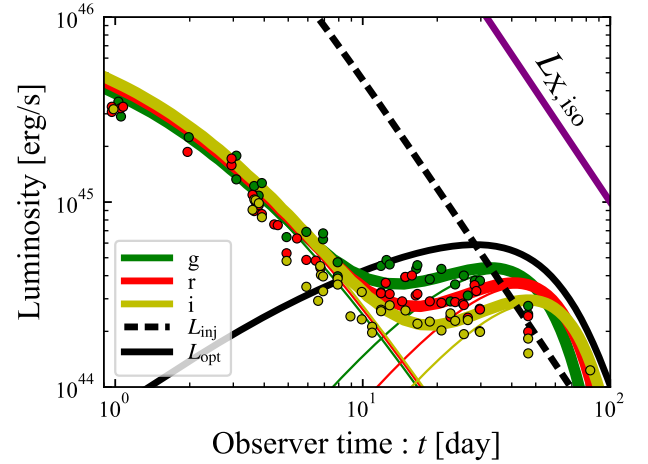


Figure 9. Combined jet afterglow and engine-powered SN model fit to the optical light curves of AT2022cmc. The g, r, and i-band light curves are shown with thick green, red, and yellow curves, respectively, and are decomposed with thinner lines into separate contributions from the jet afterglow ($t \lesssim 10$ days; §3) and SN ($t \gtrsim 10$ days). For the engine-powered SN model (Metzger et al. 2015) we assume an ejecta mass $3 M_{\odot}$, (initial) kinetic energy 10^{51} erg, and opacity $0.1 \text{ cm}^2 \text{ g}^{-1}$. Black solid and dashed curves show the bolometric optical/UV light curve of the SN and injected luminosity from the central engine, respectively. The latter is taken to be $\simeq 3\%$ of a power-law fit to the observed X-ray luminosity $L_{\text{X,iso}} = 3 \times 10^{47} \text{ erg s}^{-1} (t/5 \text{ day})^{-2}$ (purple line; see text for discussion). We note that here we show the luminosity at each wavelength, which differs from the spectral luminosity shown in Fig. 4.

stellar envelope, thus requiring a giant stellar progenitor (e.g., Quataert & Kasen 2012).

While the featureless spectra of AT 2022cmc taken during the plateau phase may pose a challenge to SN scenarios (Andreoni et al. 2022), we note that both ASASSN-15lh (Dong et al. 2016) and SN 2011kl (Greiner et al. 2015) were nearly featureless, which Mazzali et al. (2016) found could be attributed to the Doppler broadening associated with high ejecta expansion velocities $\gtrsim 20,000 \text{ km s}^{-1}$. In our best fit model shown in Fig. 9, the large energy injected by the engine at early times prior to the optical peak $\sim 10^{52}$ erg when radiation is still trapped, indeed accelerates the ejecta to high velocities $\sim 0.1 c$, even if the initial explosion possessed a lower kinetic energy.

In principle the density of the external environment as probed by the FS can also provide clues as to the nature of the central engine. In a TDE scenario, the inferred density profile $n \propto R^{-k}$ with $k \simeq 1.5 - 2$ (Fig. 2) may be the result of gas created by star formation activity locally in the nuclear star cluster (Generozov et al. 2017) or a part of an accretion flow from larger radii onto the SMBH. In particular, the measured density slope is close to the prediction $k = 1.5$ for Bondi accretion onto the SMBH (e.g., Quataert et al. 1999), in which case the density normalization $n_{17} \simeq 300 \text{ cm}^{-3}$ translates into a mass accretion rate $\dot{M} \sim 10^{-3} \dot{M}_{\text{Edd}} (M_{\text{BH}}/10^6 M_{\odot})^{-1/2}$, where \dot{M}_{Edd} is the Eddington accretion rate. This would support the nucleus of AT 2022cmc being a low-luminosity AGN (e.g., Ho 1999), which may not be surprising given the prefer-

ence for TDEs to occur in post-starburst galaxies with likely recent AGN activity (e.g., [Arcavi et al. 2014](#)) or the requirement of pre-existing magnetic flux in the galactic center environment from such a “fossil” disk in some TDE jet formation scenarios (e.g., [Tchekhovskoy et al. 2014](#); [Kelley et al. 2014](#)).

On the other hand, in the SN scenario, the density slope $k = 2$ could also be interpreted within a massive star explosion scenario as that of a stellar wind, in which case the normalization $n_{17} \simeq 300 \text{ cm}^{-3}$ would correspond to that of stellar mass-loss rate of $\dot{M} \simeq 10^{-4} M_{\odot} \text{ yr}^{-1}$ for an assumed wind velocity of 1000 km s^{-1} ($A_* \sim 10$ in the nomenclature of [Chevalier & Li 1999](#)), similar to those which characterize the circumstellar environments of core-collapse SNe (e.g., [Chevalier & Fransson 2006](#); [Chevalier 1998](#); individual SNe are shown as gray crosses in [Fig. 2](#)).

Unfortunately, then, the inferred density profile does not judicate between the two central engine models. A more promising discriminant will come from a spatially resolved location within the host galaxy which can confirm or refute a nuclear spatial location, or the detection of spectro-temporal signatures in the X-ray emission properties which distinguish a stellar-mass from supermassive compact object (e.g., [Kara et al. 2016](#)). The host galaxy properties alone may also help discriminate between the two scenarios. In particular, while the hosts of the spectrally-featureless class of optically-selected TDEs prefer to reside near or above the red edge of the green valley in the color-magnitude diagram ([Hammerstein et al. 2023](#)), the hosts of GRBs and superluminous SNe are generally bluer star-forming galaxies with low metallicity ([Lunnan et al. 2014](#); [Perley et al. 2016](#)). Another potential discriminant is the future observation of an abrupt drop in the X-ray light curve as observed in other jetted TDE candidates ([Zauderer et al. 2013](#); [Pasham et al. 2015](#)), which—if indeed the result of an accretion disk state-change occurring near the Eddington accretion rate—would not be consistent with a stellar-mass compact object.

5 SUMMARY

We have modeled the optical and radio light curves of the luminous transient AT 2022cmc to constrain the properties of the X-ray emitting jet and the density of the surrounding gaseous environment on sub-parsec scales. Our conclusions can be summarized as follows:

- Both the radio/mm emission and early optical emission ($t \lesssim 10$ days) are naturally explained by synchrotron emission from a FS blastwave which receives most of its energy during the first few days after the discovery of the transient, consistent with the duration of peak jet activity as implied by the rapidly-evolving internal X-ray emission.

- An equipartition analysis reveals that the radio/mm emitting region expands with a Lorentz factors of $\Gamma \gtrsim \text{few}$ and energy (in non-thermal electrons and the magnetic field), $E_{\text{eq}} \sim 10^{49}$ erg, into an external environment of density profile $k = 1.5\text{--}2$, broadly similar to those previously inferred for Swift J1644+57 ([Figs. 1 and 2](#)). The roughly constant energy and gradually increasing emitting particle numbers support the FS as the emitting region.

- The optical peak at 1 day is interpreted as the onset of the self-similar deceleration phase and produced by fast-cooling electrons at the FS. For a narrow jet, the total jet en-

ergy is estimated as $E_{\text{j,iso}} \sim 10^{53}$ erg with the density profile and initial Lorentz factor inferred by the equipartition analysis. This coincides with E_{eq} for an assumed beaming factor $\sim 10^{-2}$ (jet half-opening angle $\theta_j \sim 0.1$) and equipartition parameters of $\varepsilon_e \sim 0.1$ and $\varepsilon_B \sim 10^{-3}$. The observed light curve is fairly well reproduced by the FS afterglow model with these parameters. The implied X-ray radiative efficiency of the jet is high $\varepsilon_X \simeq 0.6$, also comparable to that of Swift J1644+57 ([Berger et al. 2012](#)). In contrast, a wider spreading jet is disfavored based on energetic arguments.

- Unless the jet is highly magnetized, emission from the RS should accompany the FS peak on timescales of ~ 1 day. Though the RS emission was likely not observed in AT 2022cmc, its non-appearance at optical wavelengths places a weak upper limit on the unshocked jet Lorentz factors $\Gamma_j \lesssim 100$.

- Despite the similarity of AT 2022cmc in its X-ray/radio/mm emission to other jetted TDE candidates, and its optical plateau phase to some (non-jetted) TDEs, we urge caution in cementing a TDE interpretation for this event. The location of the transient within its host galaxy has not yet been determined, the short-lived X-ray jet is an order of magnitude smaller than those of other jetted events or the debris fallback timescale for typical TDE SMBH masses $\sim 10^6 M_{\odot}$. The latter tension may be resolved for a more compact star or lower-mass SMBH, but this may be incompatible much longer duration of the highly luminous optical plateau if also powered by fall-back accretion.

- An alternative model for AT 2022cmc is a core-collapse event of a massive star giving birth to an energetic central engine (magnetar or accreting stellar-mass black hole). For an active engine timescale of $\sim 10^5$ s (spin-down time of the magnetar or fall-back time of the stellar envelope), we demonstrated that a scenario in which roughly half of the engine power goes into the X-ray emitting jet which escapes from the stellar ejecta, and half which thermalizes and boosts the luminosity of the supernova, can explain the entirety of the observations, including in the optical both the early afterglow peak and the later plateau phase ([Fig. 9](#)).

- Future observations of the host galaxy and the spatial location of the transient within the host, as well as signatures of an accretion-disk state change in the X-ray light curve, could help distinguish TDE and core-collapse scenarios for AT 2022cmc.

ACKNOWLEDGMENTS

We are grateful to Wenbin Lu for reviewing an early version of the manuscript and providing helpful comments. This work is supported in part by JSPS Overseas Research Fellowships (T.M.). B.D.M. acknowledges support from the National Science Foundation (AST-2009255).

DATA AVAILABILITY

The data underlying this article will be shared on reasonable request to the corresponding author.

REFERENCES

- Alexander K. D., van Velzen S., Horesh A., Zauderer B. A., 2020, *Space Sci. Rev.*, **216**, 81
- Andreoni I., et al., 2022, *Nature*, **612**, 430
- Arcavi I., et al., 2014, *ApJ*, **793**, 38
- Arnett W. D., 1982, *ApJ*, **253**, 785
- Barniol Duran R., Piran T., 2013, *ApJ*, **770**, 146
- Barniol Duran R., Nakar E., Piran T., 2013, *ApJ*, **772**, 78
- Bell A. R., 1978, *MNRAS*, **182**, 147
- Beniamini P., Nava L., Piran T., 2016, *MNRAS*, **461**, 51
- Berger E., Zauderer A., Pooley G. G., Soderberg A. M., Sari R., Brunthaler A., Bietenholz M. F., 2012, *ApJ*, **748**, 36
- Blandford R. D., McKee C. F., 1976, *Physics of Fluids*, **19**, 1130
- Blandford R. D., Ostriker J. P., 1978, *ApJ*, **221**, L29
- Blandford R. D., Znajek R. L., 1977, *MNRAS*, **179**, 433
- Bloom J. S., et al., 2011, *Science*, **333**, 203
- Bower G. C., Metzger B. D., Cenko S. B., Silverman J. M., Bloom J. S., 2013, *ApJ*, **763**, 84
- Bradnick B., Mandel I., Levin Y., 2017, *MNRAS*, **469**, 2042
- Bright J. S., et al., 2022, *ApJ*, **926**, 112
- Brown G. C., Levan A. J., Stanway E. R., Tanvir N. R., Cenko S. B., Berger E., Chornock R., Cucchiara A., 2015, *MNRAS*, **452**, 4297
- Bruni G., O'Connor B., Matsumoto T., Troja E., Piran T., Piro L., Ricci R., 2021, *MNRAS*, **505**, L41
- Burrows D. N., et al., 2011, *Nature*, **476**, 421
- Cendes Y., Eftekhari T., Berger E., Polisensky E., 2021a, *ApJ*, **908**, 125
- Cendes Y., Alexander K. D., Berger E., Eftekhari T., Williams P. K. G., Chornock R., 2021b, *ApJ*, **919**, 127
- Cendes Y., et al., 2022, *ApJ*, **938**, 28
- Cenko S. B., et al., 2012, *ApJ*, **753**, 77
- Chevalier R. A., 1998, *ApJ*, **499**, 810
- Chevalier R. A., Fransson C., 2006, *ApJ*, **651**, 381
- Chevalier R. A., Li Z.-Y., 1999, *ApJ*, **520**, L29
- Chevalier R. A., Li Z.-Y., 2000, *ApJ*, **536**, 195
- Cikota A., Leloudas G., Bulla M., Dai L., Maund J., Andreoni I., 2023, *ApJ*, **943**, L18
- Coughlin E. R., Begelman M. C., 2014, *ApJ*, **781**, 82
- Crumley P., Lu W., Santana R., Hernández R. A., Kumar P., Markoff S., 2016, *MNRAS*, **460**, 396
- Dai L., McKinney J. C., Roth N., Ramirez-Ruiz E., Miller M. C., 2018, *ApJ*, **859**, L20
- De Colle F., Lu W., 2020, *New Astron. Rev.*, **89**, 101538
- Dexter J., Kasen D., 2013, *ApJ*, **772**, 30
- Dong S., et al., 2016, *Science*, **351**, 257
- Eftekhari T., Berger E., Zauderer B. A., Margutti R., Alexander K. D., 2018, *ApJ*, **854**, 86
- Fong W., Berger E., Margutti R., Zauderer B. A., 2015, *ApJ*, **815**, 102
- Fuller J., Lu W., 2022, *MNRAS*, **511**, 3951
- Generozov A., Mimica P., Metzger B. D., Stone N. C., Giannios D., Aloy M. A., 2017, *MNRAS*, **464**, 2481
- Giannios D., Metzger B. D., 2011, *MNRAS*, **416**, 2102
- Giannios D., Mimica P., Aloy M. A., 2008, *A&A*, **478**, 747
- Granot J., Sari R., 2002, *ApJ*, **568**, 820
- Greiner J., et al., 2015, *Nature*, **523**, 189
- Hammerstein E., et al., 2023, *ApJ*, **942**, 9
- Hills J. G., 1975, *Nature*, **254**, 295
- Ho L. C., 1999, *ApJ*, **516**, 672
- Horesh A., Cenko S. B., Arcavi I., 2021, *Nature Astronomy*, **5**, 491
- Huang Y. F., Cheng K. S., 2003, *MNRAS*, **341**, 263
- Kara E., Miller J. M., Reynolds C., Dai L., 2016, *Nature*, **535**, 388
- Kasen D., Bildsten L., 2010, *ApJ*, **717**, 245
- Kelley L. Z., Tchekhovskoy A., Narayan R., 2014, *MNRAS*, **445**, 3919
- Keshet U., Waxman E., 2005, *Phys. Rev. Lett.*, **94**, 111102
- Kobayashi S., 2000, *ApJ*, **545**, 807
- Kobayashi S., Zhang B., 2003, *ApJ*, **597**, 455
- Krolik J. H., Piran T., 2011, *ApJ*, **743**, 134
- Leloudas G., et al., 2016, *Nature Astronomy*, **1**, 0002
- Levan A. J., et al., 2011, *Science*, **333**, 199
- Lu W., Bonnerot C., 2020, *MNRAS*, **492**, 686
- Lu W., Kumar P., 2016, *MNRAS*, **461**, L122
- Lu W., Kumar P., Narayan R., 2017, *MNRAS*, **468**, 910
- Lunnan R., et al., 2014, *ApJ*, **787**, 138
- Margalit B., Metzger B. D., Thompson T. A., Nicholl M., Sukhbold T., 2018, *MNRAS*, **475**, 2659
- Matsumoto T., Piran T., 2021a, *MNRAS*, **502**, 3385
- Matsumoto T., Piran T., 2021b, *MNRAS*, **507**, 4196
- Matsumoto T., Piran T., 2022, arXiv e-prints, p. arXiv:2211.10051
- Matsumoto T., Piran T., Krolik J. H., 2022, *MNRAS*, **511**, 5085
- Mazzali P. A., Sullivan M., Pian E., Greiner J., Kann D. A., 2016, *MNRAS*, **458**, 3455
- Metzger B. D., 2022, *ApJ*, **937**, L12
- Metzger B. D., Stone N. C., 2016, *MNRAS*, **461**, 948
- Metzger B. D., Giannios D., Mimica P., 2012, *MNRAS*, **420**, 3528
- Metzger B. D., Margalit B., Kasen D., Quataert E., 2015, *MNRAS*, **454**, 3311
- Mimica P., Giannios D., Metzger B. D., Aloy M. A., 2015, *MNRAS*, **450**, 2824
- Nakauchi D., Kashiyama K., Suwa Y., Nakamura T., 2013, *ApJ*, **778**, 67
- Pasham D. R., et al., 2015, *ApJ*, **805**, 68
- Pasham D. R., et al., 2022, *Nature Astronomy*,
- Perley D. A., et al., 2016, *ApJ*, **817**, 7
- Perlman E. S., et al., 2022, *ApJ*, **925**, 143
- Perna R., Lazzati D., Cantiello M., 2018, *ApJ*, **859**, 48
- Piran T., Svirski G., Krolik J., Cheng R. M., Shiokawa H., 2015, *ApJ*, **806**, 164
- Pushkarev A. B., Kovalev Y. Y., Lister M. L., Savolainen T., 2017, *MNRAS*, **468**, 4992
- Quataert E., Kasen D., 2012, *MNRAS*, **419**, L1
- Quataert E., Narayan R., Reid M. J., 1999, *ApJ*, **517**, L101
- Rees M. J., 1988, *Nature*, **333**, 523
- Ricci R., et al., 2021, *MNRAS*, **500**, 1708
- Ryan G., van Eerten H., MacFadyen A., Zhang B.-B., 2015, *ApJ*, **799**, 3
- Ryu T., Krolik J., Piran T., 2020, *ApJ*, **904**, 73
- Sari R., Piran T., 1995, *ApJ*, **455**, L143
- Sari R., Piran T., 1999, *ApJ*, **520**, 641
- Sari R., Piran T., Narayan R., 1998, *ApJ*, **497**, L17
- Sfaradi I., Horesh A., Fender R., Green D. A., Williams D. R. A., Bright J., Schulze S., 2022, *ApJ*, **933**, 176
- Sironi L., Giannios D., 2013, *ApJ*, **778**, 107
- Svirski G., Piran T., Krolik J., 2017, *MNRAS*, **467**, 1426
- Tchekhovskoy A., Metzger B. D., Giannios D., Kelley L. Z., 2014, *MNRAS*, **437**, 2744
- Thompson T. A., Chang P., Quataert E., 2004, *ApJ*, **611**, 380
- Vurm I., Metzger B. D., 2021, *ApJ*, **917**, 77
- Wiersema K., et al., 2012, *MNRAS*, **421**, 1942
- Wiersema K., et al., 2020, *MNRAS*, **491**, 1771
- Woosley S. E., 2010, *ApJ*, **719**, L204
- Zauderer B. A., et al., 2011, *Nature*, **476**, 425
- Zauderer B. A., Berger E., Margutti R., Pooley G. G., Sari R., Soderberg A. M., Brunthaler A., Bietenholz M. F., 2013, *ApJ*, **767**, 152
- Zhang B., Kobayashi S., 2005, *ApJ*, **628**, 315
- van Velzen S., Frail D. A., Körding E., Falcke H., 2013, *A&A*, **552**, A5
- van Velzen S., et al., 2019, *ApJ*, **872**, 198
- van Velzen S., et al., 2021, *ApJ*, **908**, 4